International Journal of Impact Engineering, (2014), 73, 43-55.
DOI: http://dx.doi.org/10.1016/j.ijimpeng.2014.06.005

Approaching steady cavitation: The time scale in hypervelocity cavity expansion in work hardening and transformation hardening solids

J.A. Rodríguez-Martínez [a, *], T. Cohen [b], R. Zaera [a]

[a] *Department of Continuum Mechanics and Structural Analysis, University Carlos III of Madrid, Avda. de la Universidad, 30, 28911 Legan´es, Madrid, Spain* [b] *Department of Mechanical Engineering, Massachusetts Institute of Technology, Cambridge, MA 02139, USA*

*Corresponding author. Tel.: +34 916248460; fax: +34 916249430. *E-mail address:* jarmarti@ing.uc3m.es (J.A. Rodríguez-Martínez).

Abstract: The extreme phenomena of dynamic cavitation is studied both theoretically and numerically for two families of strain hardening materials. Though analytical results are limited to the steady, self-similar expansion state, the numerical approach facilitates investigation of the transient response, including evaluation of the time required to approach the steady-state limit. While recent studies show that shock waves may appear in hypervelocity cavity expansion fields, the present study suggests a numerical model which can capture the appearance and evolution of these shock waves. That model is validated by comparison with theoretical results at the steady-state limit, thus facilitating future investigation of the dynamic response for materials with more complicated constitutive behavior, for which theoretical re-sults are limited. The constitutive sensitivities are also examined, showing that the specific hardening response of the material has little effect on the cavitation response.

Keywords: Finite strains, Shock waves, Cavity expansion, Work hardening, Transformation hardening.

1. Introduction

Cavitation instability arises when an embedded cavity, within the solid, expands spontaneously upon application of constant load, subjected either at the cavity wall or in the remote field. That critical level of load, to induce cavitation, is the quasistatic cavitation pressure. If the applied load is higher than that critical level then dynamic cavitation will evolve implying that the cavity expands with finite velocity. If the applied load is lower than that critical level then the solid will find a new configuration of static equilibrium.

Over the years, cavitation phenomena has been widely accepted as a basic mode of failure in solids. Following the early study by Bishop et al. [1], which suggested that the resisting pressure in the indentation process is the spherical quasistatic cavitation pressure, extensive research has been devoted to the relation between cavitation phenomena and other material instabilities, including penetration and perforation phenomena and fracture initiation. Cavitation has been experimentally observed in a variety of materials ranging from ductile metals [2], to biological soft tissue [3]. Though most available research on cavitation phenomena focuses on quasistatic fields (see an extensive review by Horgan and Polignone [4] for hyperelastic solids and by Cohen et al. [5] for elastoplastic solids), it is understood that high velocity penetration processes are related to dynamic cavitation [6].

Available theoretical studies on dynamic spherical cavity expansion [7–12] focus on hardening and non-hardening elastoplastic solids and pressure sensitive materials. In those studies the theoretical formulation of the field response bypasses the transient behavior by assuming a self-similar expansion. While most studies on dynamic cavity expansion are limited to moderate velocities, it was recently shown, in Refs. [11,12], that at hypervelocities plastic shock waves may appear. Therein the dynamic response is fully accounted for by exposure of a singularity in the governing field equations and application of Hugoniot jump conditions. Ortiz and Molinari [13] studied the strain rate effects in dynamic spherical cavity expansion for incompressible hardening elastoplastic solids, thus accounting for the transient response but without the appearance of shock waves.

It is conceivable that the appearance of shock waves in the material response can have a dramatic effect on the resistance of the solid to penetration, and it is therefore essential to obtain an in depth understanding on the evolution of these shock waves. Hence, the present study attempts at a computational model of dynamic cavitation which agrees with the theoretical models at the steady-state limit and is able to predict the transient behavior, including the time required for appearance of the theoretical steady-state response. Once that model is verified it can be extended to

account for more complicated material response for which theoretical predictions do not exist, including strain rate effects and thermo-mechanical coupling.

In the present study a computational model is developed and compared with results obtained according to the theoretical framework for dynamic spherical cavity expansion proposed in Refs. [8,10,11]. First, a work hardening material response is considered, similar to that in Cohen et al. [11], then the model is extended for a family of *strain induced martensitic transformation* (SIMT) materials for which theoretical modeling is limited. While the first hardening mechanism accounts for strengthening of the material by dislocations accumulation, the second one is equivalent to a dynamic composite effect due to the progressive transformation of austenite (softer phase) to martensite (harder phase) upon deformation. This is a characteristic of multiphase TRIP steels and metastable austenitic grades, that are widely used for energy absorption in crash or blast protection applications [14–18]. It has to be noted that the behavior of solids showing martensitic transformation at high strain rates has been recently analyzed in perforation [19] and dynamic necking [20,21] problems. These works identified loading conditions and characteristics of transformation kinetics for which martensitic transformation delays plastic localization and boosts the energy absorption capacity of the material. However, little is known about the role played by martensitic transformation in development of cavitation instabilities.

The hardening response of metal alloys plays an important role in their application to protective structures due to increased energy absorbing capabilities. On that note, appearance of plastic shock waves is also necessarily involved with dissipation due to entropy rise manifested by a jump in temperature across the shock [22,23]. Hence, better understanding of the role of shock waves in the dynamic material response, and the related constitutive sensitivities, can lead to development of more efficient protective materials in the future.

Rosenberg and Dekel [24] presented a 2D numerical investigation of the dynamic cavitation response of perfectly plastic materials in the context of long-rod penetration mechanics. In the present work we extend that numerical framework to more complicated material response and at hypervelocities to observe the appearance of plastic shock waves. An essential feature of the present study is in understanding the transient response, or namely, the time required to approach the steady field. Since steady cavitation fields are being applied in prediction of penetration and perforation [24,25], it is important to understand the relevant time scales. If the penetration process is much faster than the time required for steady cavity expansion to appear then steady cavita-tion fields are not sufficient in underlying the physical phenomena.

As described in Section 2, the constitutive model is based on the standard principle of Huber–Mises plasticity accounting for finite strains and two different strain hardening mechanisms: work hardening and martensitic transformation hardening. Work hardening materials are defined by a simple Ludwik hardening law, whereas transformation hardening materials are described as in Zaera et al. [21]. In Section 3 we shortly recapitulate the analytical investigation of the steady cavitation fields for arbitrary hardening response, with earlier reference to Durban and Fleck [8] and Masri and Durban [10]. The appearance of shock wave discontinuity and application of jump conditions at the shock is accounted for as in Cohen et al. [11] and Cohen and Durban [12]. The numerical model is presented in Section 4, followed by analysis and results in Sections 5 and 6. Section 5 focuses on the evolution of the steady field and shock wave propagation, and Section 6 examines the constitutive sensitivities. Section 7 outlines the main outcomes of this study.

2. Constitutive model

As stated before, to obtain a better understanding of the constitutive sensitivity of dynamic cavitation, we consider two different strain hardening mechanisms: work hardening and martensitic transformation hardening. The main hypothesis of the constitutive models used in the present analysis centers on the standard principles of Huber–Mises plasticity: hypoelastic behavior, additive decomposition of the rate of deformation tensor, isotropic hardening, associated flow rule and plastic power equivalence

$$\boldsymbol{\sigma}^{\nabla} = \mathbf{C} : \mathbf{d}^{e} = \mathbf{C} : (\mathbf{d} - \mathbf{d}^{p}) \tag{1}$$

$$\Psi = \overline{\sigma} - \sigma_Y = 0 \tag{2}$$

$$\mathbf{d}^{p} = \frac{\partial \Psi}{\partial \boldsymbol{\sigma}} \dot{\bar{\varepsilon}}^{p} = \frac{3\mathbf{s}}{2\overline{\sigma}} \dot{\bar{\varepsilon}}^{p} \tag{3}$$

where $\boldsymbol{\sigma}^{\nabla}$ is an objective derivative of the Cauchy stress tensor, $\mathbf{d}$, $\mathbf{d}^{e}$ and $\mathbf{d}^{p}$ are the total, elastic, and plastic rate of deformation tensors respectively, $\mathbf{C}$ is the Hooke tensor for isotropic elasticity (defined by Young modulus E and Poisson ratio ν), Ψ the yield function, $\overline{\sigma}$ the equivalent stress, $\dot{\bar{\varepsilon}}^{p}$ the equivalent plastic strain rate, σ_Y is the yield stress and $\mathbf{s}$ the deviatoric stress tensor. The reference values that will be considered for E, ν, as well as for initial mass density, are given in Table 1.

Next, we present the models used to describe the two aforementioned hardening processes. It is worth noting that both processes have been intentionally uncoupled in our study in order to uncover separately the influence of each one in the process of cavity expansion. Thus, plastic strain has been considered as the unique source of work hardening, whereas phase transformation has been considered as the unique source of transformation hardening. Certainly both effects are ultimately triggered by plastic deformation, but the functional dependence of the yield stress on strain greatly differs among them.

2.1. Work hardening material

For the work hardening material, the value of the yield stress is given as a function of the equivalent plastic strain $\bar{\varepsilon}^{p}$ through a widely used power law (frequently referred to as the Ludwik hardening law)

$$\sigma_Y = A + B(\bar{\varepsilon}^{p})^{k} \tag{4}$$

The reference values of the material parameters A, B and k are given in Table 2.

2.2. Transformation hardening material

Based on the earlier study by Olson and Cohen [26] and assuming that intersection of shear bands in the austenite is the dominant mechanism of SIMT, we suggest a model which captures the martensitic transformation by considering the closed-form

Table 1
Reference elastic properties and density for work hardening and transformation hardening materials.

Symbol	Property and units	Value
E	Young modulus (GPa)	200
ν	Poisson ratio	0.33
ρ_o	Initial density (kg/m^3)	7800

Table 2
Reference parameters for the power law, Eq. (4).

Symbol	Property and units	Value
A	Initial yield stress (MPa), Eq. (4)	500
B	Work hardening modulus (MPa), Eq. (4)	500
k	Work hardening exponent, Eq. (4)	0.5

relation between the volumetric fraction of martensite f_m and the plastic strain in the austenite $\bar{\varepsilon}_a^p$

$$f_m = 1 - \exp\Big[-\beta\big(1 - \exp(-\alpha\bar{\varepsilon}_a^p)\big)^n\Big] \tag{5}$$

here n is the exponent relating shear bands with shear band intersections through a power law, α is a temperature dependent parameter representing the rate of shear-band formation and β a temperature dependent parameter proportional to the probability that a shear band intersection will form an embryo. The strain as well as the strain rate of the austenite are quite close to the homogenized ones and much larger than those corresponding to the martensite [27]. Therefore, based on Zaera et al. [21], the plastic deformation in the austenite $\bar{\varepsilon}_a^p$ and the plastic deformation of the steel $\bar{\varepsilon}^p$ are considered equivalent in the current approach, and Eq. (5) leads to

$$f_m = 1 - \exp\big[-\beta(1 - \exp(-\alpha\bar{\varepsilon}^p))^n\big] \tag{6}$$

The closed-form solution provided by Eq. (6) to capture the dependence of the transformed martensite in terms of strain, instead of using an evolution law, presents the advantage of its simplicity, specifically for analytical approaches like the self-similar theory for cavity expansion that will be presented in the next section.

Following Zaera et al. [21], the effective yield stress in the two-phase steel σ_Y is calculated by the rule of mixtures

$$\sigma_Y = (1 - f_m)\sigma_Y^a + f_m\sigma_Y^m \tag{7}$$

where σ_Y^a and σ_Y^m are the yield stress of the austenite and of the martensite respectively. The previous expression highlights the effect of martensitic transformation as unique source of hardening that, according to the perfect-plasticity hypothesis adopted for the phases, can be denoted as *transformation hardening*.

Table 3 shows the reference values of the parameters for the SIMT model, representative of a metastable austenitic steel.

3. Theoretical model

We consider the dynamic expansion of a spherical cavity, in an infinite medium, by subjecting constant pressure at the cavity wall. Though the plastic deformation is incompressible, elastic compressibility implies that the disturbance, imposed by the expanding cavity, is carried outwards along the spatial radial coordinate R at finite velocity. Considering materials with a definite yield point, that velocity is the wave velocity of the elastic precursor behind which an elastic range develops, as illustrated on Fig. 1. I f the applied pressure is sufficient to induce plasticity then an interface between the elastic range and elastoplastic range follows the elastic wave. For even higher levels of applied pressure, to induce hypervelocity expansion of the cavity, a plastic shock wave may appear in the elastoplastic range, characterized by a jump in field variables [11,12].

Table 3
Parameters related to SIMT model taken from Zaera et al. [21], Eqs. (6) and (7).

Symbol	Property and units	Value
n	Dimensionless material constant, Eq. (6)	4.5
α	Dimensionless material constant, Eq. (6)	7.943
β	Dimensionless material constant, Eq. (6)	1.204
σ_Y^a	Yield stress of the austenite (MPa), Eq. (7)	300
σ_Y^m	Yield stress of the martensite (MPa), Eq. (7)	900

The theoretical formulation presented in Masri and Durban [10] and Cohen et al. [11] accounts for an arbitrary strain hardening response. Hence, we briefly recapitulate that formulation here, in the present notation. To bypass the transient response and obtain the self-similar expansion field it is assumed that all field variables depend only on the similarity parameter $\xi = R/A$ as the independent variable, where A is the current hole radius. Therefore transformation of field equations (i.e. equation of motion, constitutive relations and conservation of matter) reduces to a system of two differential equations

$$(1-2\nu)\Sigma_r' + (1-\nu)\Sigma' + \frac{1}{2}\bar{\varepsilon}^{p\prime} = \frac{1}{\xi}\left(1 - e^{\Phi}\right) \tag{8}$$

$$\Sigma_r' - m^2\xi^2\Big((1-2\nu)\Sigma_r' - 2\nu\Sigma' - \bar{\varepsilon}^{p\prime}\Big)e^{-\Theta-2\Phi} = \frac{2}{\xi}\Sigma \tag{9}$$

with two closed-form relations for the density ratio and the velocity

$$\frac{\rho}{\rho_o} = e^{-\Theta}, \quad V = \xi\left(1 - e^{-\Phi}\right) \tag{10}$$

respectively, where

$$\Theta = 3(1-2\nu)\Sigma_h, \quad 2\Phi = 2(1+\nu)\Sigma + 3\bar{\varepsilon}^p \tag{11}$$

here the superposed prime represents differentiation with respect to ξ, the dimensionless radial, equivalent and hydrostatic stresses are $(\Sigma_r, \Sigma, \Sigma_h) = (\sigma_r, \overline{\sigma}, \sigma_h)/E$ respectively, ρ is the current density, the velocity is dimensionless according to $V = \dot{R}/\dot{A}$, where the

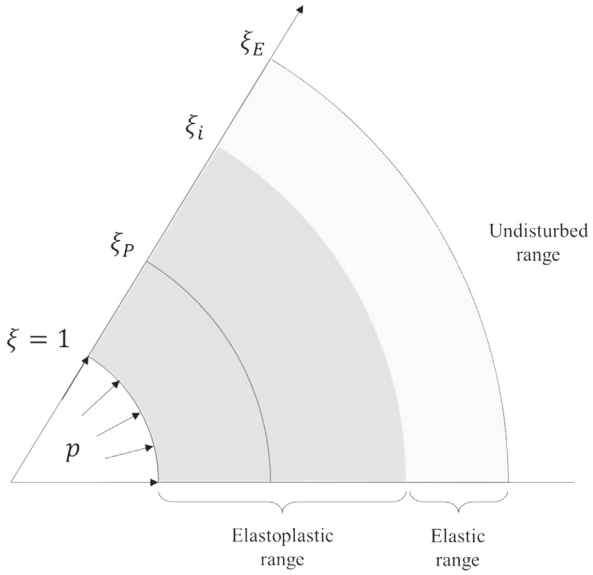

Fig. 1. Illustration of the steady cavity expansion field. The internal pressure p is applied at the cavity wall where the dimensionless radial coordinate $\xi = R/A = 1$. The remote field, at $\xi > \xi_E$, is undisturbed while behind the elastic wave, at $\xi = \xi_E$, an elastic range develops. The transition between the elastic and elastoplastic regions is denoted by ξ_i and ξ_P denotes the plastic shock wave.

superposed dot represents differentiation with respect to time, and the dimensionless cavity expansion velocity (with respect to the wave velocity in a linearly elastic rod) is defined by

$$m = \frac{\dot{A}}{\sqrt{E/\rho_o}} \tag{12}$$

Given a relation between the equivalent stress and the plastic strain, as those defined in Section 2, the present system of equations is sufficient to describe the steady-state cavity expansion process. Hence, for a given expansion velocity m, integration of the equations with proper boundary conditions (obtained by shooting method, see further details in Cohen et al. [11]), will admit the matching cavitation pressure $p = -\sigma_r$ ($\xi = 1$).

A closed-form solution for the elastic range was obtained by Durban and Masri [9], showing that the dimensionless elastic wave velocity is

$$C_E = m\xi_E = \sqrt{\frac{1-\nu}{(1-2\nu)(1+\nu)}} \tag{13}$$

in agreement with the known linearly elastic wave speed, where ξ_E represents the location of the elastic wave along the dimensionless radial coordinate ξ.

It was shown in Cohen et al. [11] that for high expansion ve-locities the system of equations (8) and (9) may become singular if

$$(1-2\nu)m^2\xi^2 = \frac{1+(1-2\nu)h}{3-(1-2\nu)h}e^{\Theta+2\Phi} \tag{14}$$

where $h = (1 + \mathrm{d}\bar{\varepsilon}^p/\mathrm{d}\Sigma)^{-1}$ is the nondimensional tangent modulus of the stress strain curve. That singularity imposes possible appearance of discontinuity in the field variables, namely a plastic shock wave. At the discontinuity, the field equations must be replaced with jump conditions. The fundamental relations are the Hugoniot jump conditions,

$$[\![2\nu\Sigma_r + 2(1-\nu)\Sigma_\theta + \bar{\varepsilon}^p]\!] = 0 \tag{15}$$

$$[\![\Theta + \Phi]\!] = 0 \tag{16}$$

requiring conservation of mass and momentum, respectively.

Specifically for the limit case of an elastic/perfectly plastic material the solution in Cohen et al. [11] shows that the plastic shock wave settles on the interface between the elastic range and the plastic range. Since no singularity in the field equations is detected in the elastic range, it was not possible to obtain consistent jump conditions across the shock. It should be noted, however, that inserting *minimal levels* of material hardening into the constitutive model can facilitate an analytical solution.

4. Finite element model

This section describes the features of the axisymmetric finite element model developed to simulate dynamic spherical cavity expansion. The numerical analyses are carried out using the finite element program ABAQUS/Explicit [28]. Geometry and dimensions of the finite element model are based on Rosenberg and Dekel [24]. The problem setting is of a very large sphere of radius $R_s = 300$ mm with a small cavity in its center of radius $R_c = 0.5$ mm. Due to the symmetry of the model, only the $\theta \geq 0$ half of the specimen has been analyzed (see Fig. 2). The solid is initially at rest while a constant internal pressure p is applied at the cavity wall. It has to be noted that the chosen dimensions (radius) of the sphere and the cavity do not influence the simu-lation results. It has been systematically verified that the stress waves generated by application of the cavity pressure are reflected from the free boundary much later than the development of a steady cavitation field. As in the theoretical model, thermal effects are not considered.

The model has been meshed using a total of 240,000 four-node axisymmetric reduced integration elements, CAX4R in ABAQUS notation. This number of elements results from placing 200 elements along the circumferential direction and 1200 along the radial direction. The mesh shows radial symmetry in an attempt to retain the symmetry of the problem and minimize the potential interference of the mesh on the calculations. The elements size is constant along the circumferential direction

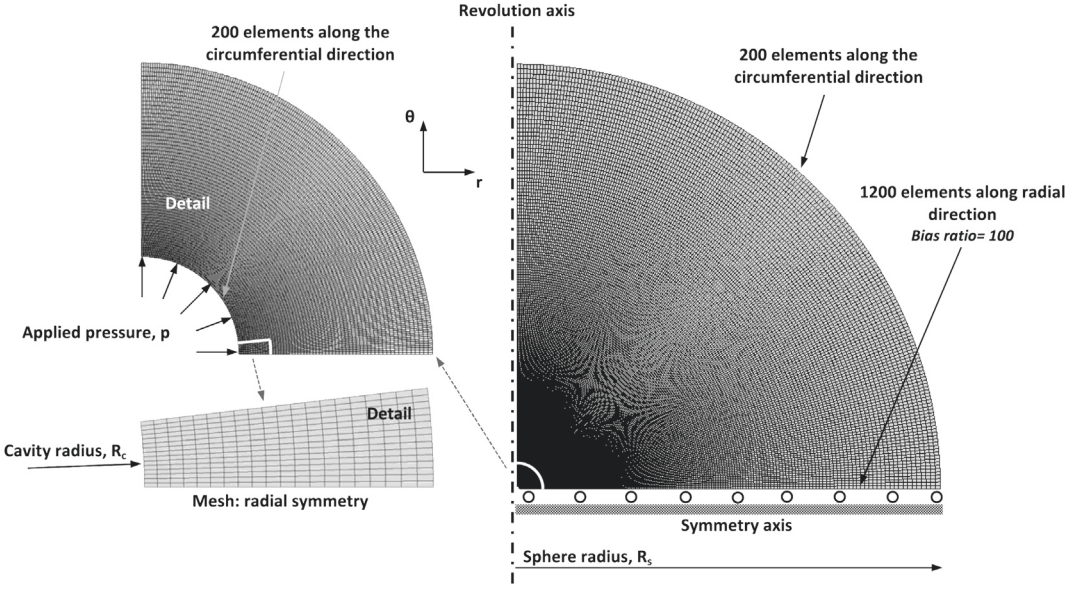

Fig. 2. Axisymmetric finite element model developed to analyze dynamic spherical cavity expansion.

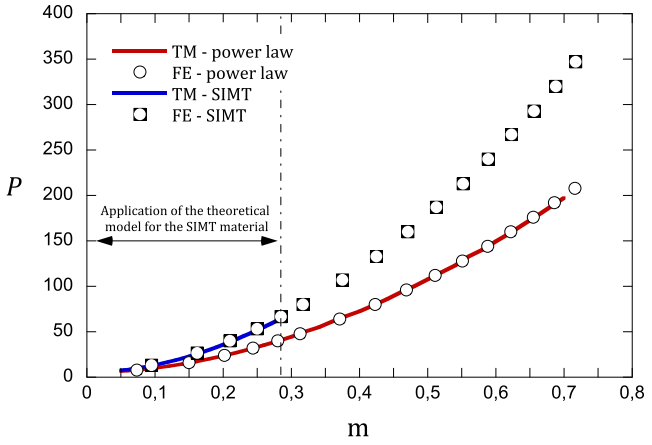

Fig. 3. Variation in dimensionless applied pressure P with dimensionless cavitation velocity m for work hardening (power law) and transformation hardening (SIMT) materials. Comparison between theoretical model (TM) and finite element results (FE) for reference material parameters.

whereas it decreases along the radial direction as the cavity is approached. Namely, along the radial direction the elements show a bias ratio of 100. Thus, small elements with dimensions 12 μm × 4 μm are defined near the cavity, to capture high gradients of stress and strain which are expected to arise in that region. Furthermore, these high gradients of stress and strain may lead to severe mesh distortion. In order to prevent this drawback, the Arbitrary Lagrangian Eulerian (ALE) adaptive meshing available in ABAQUS has been applied to the entire model. ALE adaptive meshing uses a single mesh definition that is gradually smoothed within analysis steps. The frequency of adaptive meshing is set to 1 and the remeshing sweeps per increment are set to 10. These values of the controlling parameters of the adaptive meshing are checked to be suitable to ensure a proper aspect ratio of the elements during the computations. A mesh convergence study has been performed, and the time evolution of different critical output variables, namely stress, strain and cavitation velocity were compared against a measure of mesh density until the results converged satisfactorily.

The set of constitutive equations describing the material behaviors presented in Section 2 are implemented in the finite element code through a user subroutine. For its integration in a finite deformation framework, incremental objectivity is achieved by rewriting them in a corotational configuration [29,30], d e fined in ABAQUS/Explicit by the polar rotation tensor. The stress is updated with the radial return algorithm

$$\boldsymbol{\sigma}_{n+1} = \boldsymbol{\sigma}^{\text{trial}}_{n+1} - 3G\Delta\bar{\varepsilon}^{p}\frac{\mathbf{s}_{n+1}}{\bar{\sigma}_{n+1}} \tag{17}$$

where the trial stress is defined by

$$\boldsymbol{\sigma}^{\text{trial}}_{n+1} = \boldsymbol{\sigma}_{n} + \mathbf{C} : \Delta\boldsymbol{\varepsilon} \tag{18}$$

According to the properties of radial return, the equivalent stress may be updated with the following equation

$$\bar{\sigma}_{n+1} = \bar{\sigma}^{\text{trial}}_{n+1} - 3G\Delta\bar{\varepsilon}^{p} \tag{19}$$

and the yield condition Eq. (2) which, coupled to Eq. (4) in the case of the work hardening material and Eq. (7) in the case of the transformation hardening material, permits to obtain the equivalent plastic strain increment $\Delta\bar{\varepsilon}^{p}$.

In the next sections, results obtained from the theoretical model and the finite element simulations are presented. It has to be mentioned that extremely high levels of applied pressure are investigated, in a range where the ability of the material to endure such load levels may be questionable. Nevertheless, exploring high pressure cavitation fields is justified for the sake of better understanding of the essential phenomena involved in dynamic cavitation problems.

The following analysis is composed of two parts. We begin by focusing on the dynamic development of a steady self-similar field including possible appearance of plastic shock waves beyond a critical cavitation velocity. Then we examine the influence of the constitutive equation in the dynamic deformation field. Throughout the analysis, comparison between analytical results and the numerical model is conducted and results are shown for both work hardening and transformation hardening solids.

5. Analysis and results: self-similar fields and plastic shock waves

Cavitation fields, which are characterized by steady expansion of an embedded cavity due to application of internal pressure at the cavity wall, are necessarily involved with high levels of strains and high gradients with possible appearance of plastic shock waves at hypervelocities [11,12]. Therefore, to verify the application of the suggested numerical approach to model such extreme material behavior it is essential, as a first step, to compare the numerical results with analytical solutions. That numerical model can then be

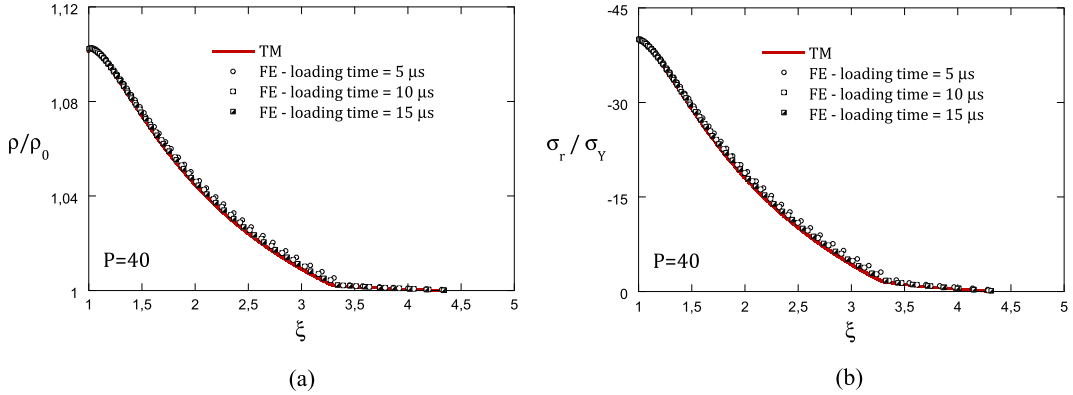

Fig. 4. Work hardening material (power law). Variation along the normalized radial coordinate ξ of: (a) density ratio ρ/ρ_0 and (b) dimensionless radial stress σ_r/σ_Y. Comparison between theoretical model (TM) and finite element results (FE) for $P = 40$. Finite element results are shown for different loading times: 5 μs, 10 μs and 15 μs.

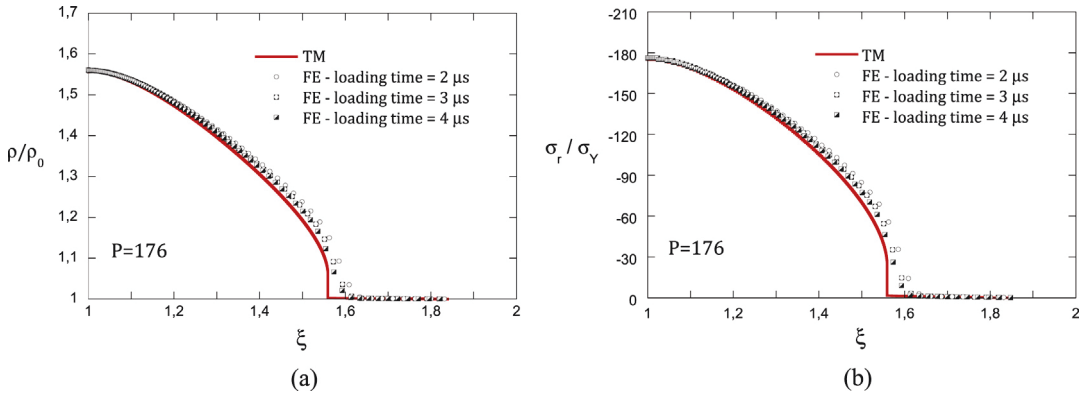

Fig. 5. Work hardening material (power law). Variation along the normalized radial coordinate ξ of: (a) density ratio ρ/ρ_0 and (b) dimensionless radial stress σ_r/σ_Y. Comparison between theoretical model (TM) and finite element results (FE) for $P = 176$. Finite element results are shown for different loading times 2 μs, 3 μs and 4 μs.

extended to include more complex material response for which analytical solutions are not available.

Theoretical solutions of dynamic cavitation fields [11,12] bypass the transient dynamic behavior to obtain only the steady self-similar response. However, to obtain the steady field via finite element simulations, the transient behavior can not be avoided and initial conditions must be defined. In this respect, we have checked that the limit steady-state expansion field is not sensitive to the loading path. This implies an eigenvalue problem relating the steady expansion velocity with the applied pressure. That relation can then be compared with the analytical results. Hence, the numerical model can provide information on the evolution of the steady field, and more specifically an estimation of the time it takes for the steady field to evolve.

The finite element simulations presented in this paper consider a solid, initially at rest, subjected to sudden application of a constant pressure. If that pressure is below a critical value, the velocity of the cavity wall rises quickly and just after decays to zero since the solid is able to find a new configuration of static equilibrium. For pressures above that critical value, the velocity of the cavity wall rises with time approaching a finite value asymptotically. Therefore, for a given applied pressure, the numerical computations provide the cavitation velocity and an estimation of the time required to reach it.

Relations between the dimensionless cavitation pressure $P = p/\sigma_Y$ and the dimensionless cavity expansion velocity m are shown on Fig. 3 for both work hardening (power law) and transformation hardening (SIMT) materials with reference parameters listed in Tables 1–3. Results are presented within a wide range of cavitation velocities $0.05 \lesssim m \lesssim 0.75$ for both theoretical and numerical models. As expected in view of available results [9,10,24], the cavity pressure is an increasing power-type concave-up function of the cavity expansion velocity. Agreement between the theoretical model and the finite element computations is shown. However, the theoretical prediction of cavitation in the SIMT material is limited to $m \lesssim 0.28$. The theoretical model predicts that at $m \simeq 0.28$ a plastic shock wave will appear and since the different phases of the SIMT material are non-hardening, that shock wave will settle on the interface between the plastic zone and the elastic zone [11]. Hence, it is not possible to obtain consistent jump conditions across the shock discontinuity and the analytical solution is limited as explained in Section 3.

The numerical simulations predict that, for the lowest cavitation velocity investigated, the time required to reach the steady-state is ~2.5 μs whereas for the greatest cavitation velocity considered the time required to reach the steady-state is ~0.4 μs. That result is similar for both types of hardening materials, implying that the inelastic behavior has little influence on the time required to reach the steady-state expansion, at least for the loading configuration and material behaviors selected in this paper. We will further elaborate on this point in Section 6.

Next, we pay specific attention to the development of a self-similar field and the appearance of plastic shock waves when a critical cavitation velocity is exceeded. For the sake of clarity, we

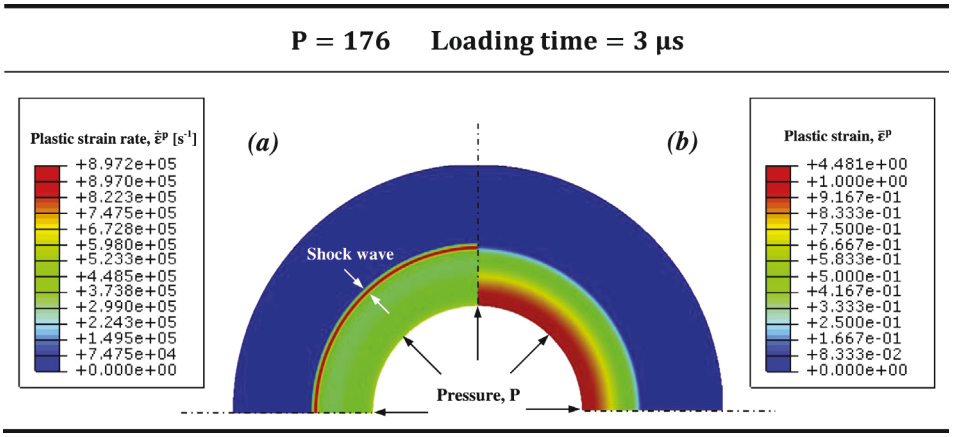

Fig. 6. Finite element results. Work hardening material (power law). Detail of the zone surrounding the cavity. Cavitation fields for $P = 176$ and loading time 3 μs: (a) plastic strain rate $\dot{\bar{\varepsilon}}^p$ and (b) plastic strain $\bar{\varepsilon}^p$.

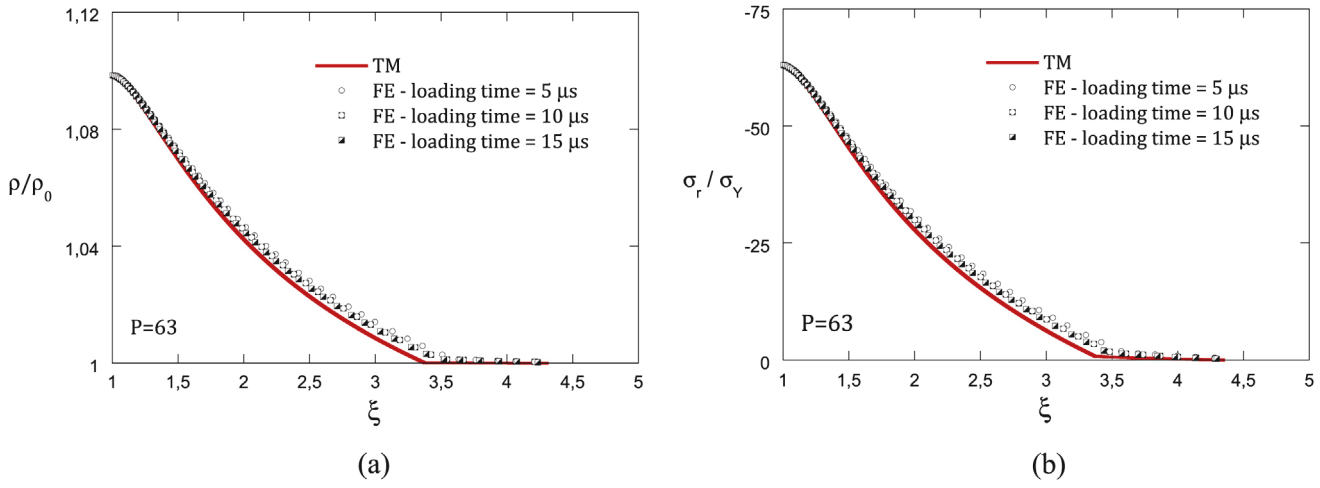

Fig. 7. Transformation hardening material (SIMT). Variation along the normalized radial coordinate ξ of: (a) density ratio ρ/ρ_0 and (b) dimensionless radial stress σ_r/σ_Y. Comparison between theoretical (TM) model and finite element results (FE) for $P = 63$. Finite element results are shown for different loading times 5 μs, 10 μs and 15 μs.

discuss the results separately for the work hardening and the transformation hardening solids.

5.1. Work hardening material (power law)

Variation of the density ratio ρ/ρ_0 and the dimensionless radial stress σ_r/σ_Y along the normalized radial coordinate $\xi = R/A$ are shown on Fig. 4 for $P = 40$ (which corresponds to $m = 0.28$). Predictions of the theoretical model are confronted with results obtained from the finite element calculations. The latter have been obtained for three different loading times (5 μs, 10 μs and 15 μs) for which the cavitation velocity has already been reached. Agreement between the theoretical model and the finite element calculations is shown. Furthermore, the differences between finite element results corresponding to different loading times are practically negligible. Thus confirming the self-similarity of the cavitation field which, in turn, is a fundamental hypothesis for development of the theoretical model as discussed in Section 3. It should be noted that the theoretical model predicts decrease in density at the very near vicinity of the cavity which can only be observed by enlargement of the figure in that area, see Cohen et al. [11]. That behavior is accompanied by infinite values of strain and effective stress owing to singularity of the self-similar field at $\xi = 1$ [11,12]. However, discretization of the solid impedes to expose this singularity in the computational model. The element size imposes a limit to the characteristic length scale of the phenomena which can be described by the numerical simulations.

In Fig. 4(a) we see that near the cavity the maximum density ratio is $\rho/\rho_0 \approx 1.1$. As we move away from the cavity the material density *smoothly* decreases as a concave-up power-type function. For $\xi \approx 3.30$ we observe a change in the slope of the curve which defines the elastoplastic interface. For $\xi > 3.30$ the field is elastic and extends up to $\xi_E \approx 4.43$ where $\rho/\rho_0 = 1$, i.e. for values of $\xi > 4.43$ the solid is undisturbed. The location of the rigid/elastic front ob-tained from the numerical computations can only be observed by enlargement of the figure in that area. This value of $\xi_E \approx 4.43$, obtained from the finite element computations, is very close to 4.35, which is the theoretical value obtained from Eq. (13). The small difference could be attributed to the discretization and to the artificial dissipative effects (viscosity) included by the finite element code. The cavitation pressure is observed on Fig. 4(b) near the cavity wall ($\xi = 1$) where $P = -\sigma_r/\sigma_Y = 40$.

Fig. 5 presents results similar to those in Fig. 4, but considers a much larger value of the applied pressure $P = 176$ (which

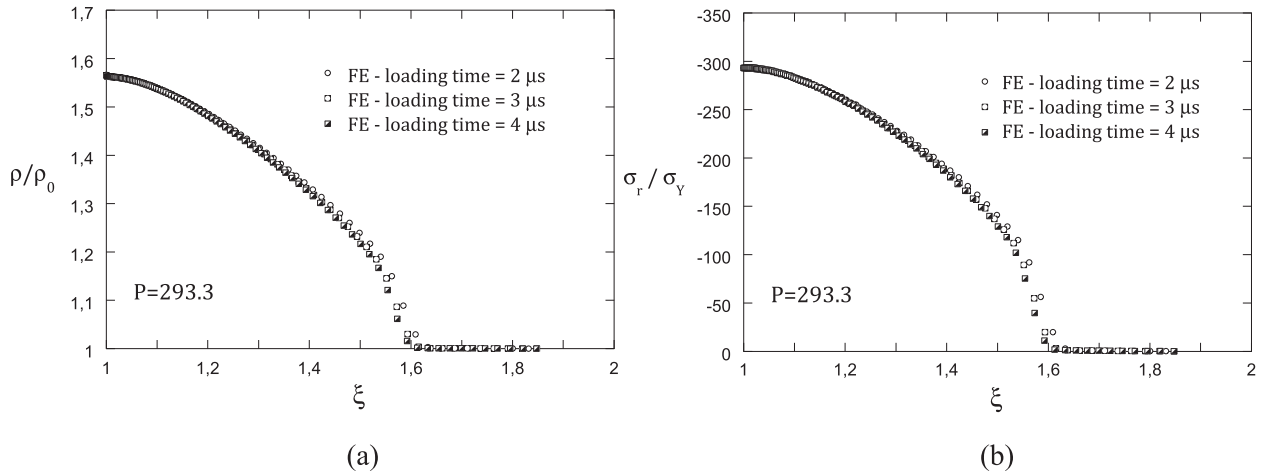

Fig. 8. Transformation hardening material (SIMT). Variation along the normalized radial coordinate ξ of: (a) density ratio ρ/ρ_0 and (b) dimensionless radial stress σ_r/σ_Y. Finite element results (FE) for $P = 293.3$. Finite element results are shown for different loading times 2 μs, 3 μs and 4 μs.

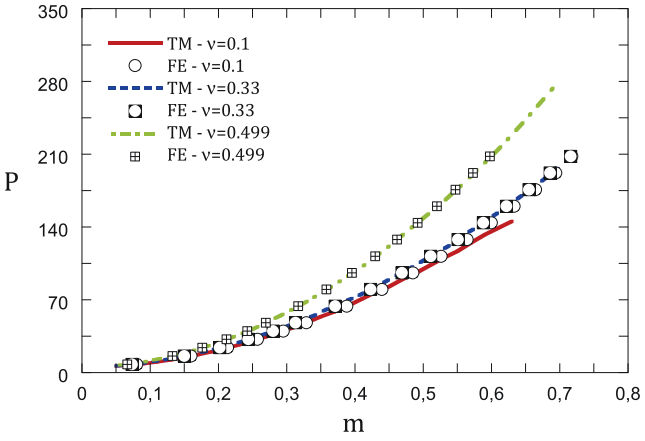

Fig. 9. Work hardening material (power law). Variation in dimensionless applied pressure P with dimensionless cavitation velocity m for $\nu = 0.1$, $\nu = 0.33$ (reference material) and $\nu = 0.499$. Comparison between theoretical model (TM) and finite element (FE) results.

corresponds to $m = 0.66$). Nevertheless, it is observed that the agreement between the theoretical model and the finite element computations is maintained. Finite element results are shown for 2 μs, 3 μs and 4 μs. Differences between the computation results for the different times are minimal, implying that a self-similar cavitation field develops as assumed in the theoretical approach. We anticipate that FE calculations confirm self-similarity of the cavitation fields, for all the applied pressures and material behaviors investigated in this paper. As expected, comparison of these results with those presented in Fig. 4 illustrate that material density and radial stress near the cavity wall increase with applied pressure. It has to be noted that, unlike the curves for $P = 40$, on Fig. 5 the ratios ρ/ρ_0 and σ_r/σ_Y evolve with ξ as concave-down power-type functions. Approaching $\xi \approx 1.6$, from the cavity wall, we observe a sudden decrease in ρ/ρ_0 and σ_r/σ_Y and then a change in slope which corresponds to the interface between the elastoplastic range and the elastic range. By comparison with the results reported in Fig. 4, w e see that the value of ξ which determines the elastoplastic interface decreases with applied pressure. The rapid decrease in ρ/ρ_0 and σ_r/σ_Y detected close to $\xi \approx 1.6$ is caused by the emergence of a plastic shock wave. It has been observed that the shock intensifies with increasing cavitation velocity, while the first shock appears for expansion velocity $m = 0.56$. Furthermore, the plastic shock wave moves toward the elastoplastic interface as the cavitation velocity increases [11]. For a more detailed discussion on the theoretical background on appearance of shock waves in cavitation see Refs. [11,12]. Moreover, for values of $\xi > 1.6$ we have the elastic field which extends to $\xi_E = 1.84$ (the rigid/elastic front can only be observed by enlargement of the figure in that area). This latter value defines the velocity of the elastic precursor which propagates into the undis-turbed material. The value of ξ_E obtained from the finite element computations is very close to 1.86, which is obtained from Eq. (13).

While the theoretical model unequivocally determines the shock wave by prescribing jump conditions at the onset of singularity in the governing equations (see Section 3 for details), in the finite element simulations such discontinuity in the field variables is not observed but rather what can be named as a *steep gradient*. Hence, FE computations predict a finite width of the shock wave which is, at a some extent, controlled by the element size (see Zukas and Scheffer [31]). Despite that inherent mesh dependency, agreement with theoretical results is observed while the only difference is in smoothening the computational results in the vicinity of the shock wave.

Detailed contours of plastic strain rate and plastic strain in the zone surrounding the cavity are obtained via the finite element model at 3 μs and presented on Fig. 6 for $P = 176$. It is shown that, near the cavity wall, strain rate values are up to 7×10^5 s^{-1}. The deformation rate monotonically decreases as we move outwards along the radial direction. Nevertheless, at a certain distance from the cavity a drastic increase of strain rate appears. This increase, which is limited to a narrow band, illustrates the emergence of the shock wave which leads to prediction of plastic strain rates of up to ~9×10^5 s^{-1}. From the plastic strain contours we deduce that the shock wave is located near the elastoplastic interface, where the plastic strains suddenly drop from a finite value to zero. Moreover, as anticipated in Section 4, high levels and high gradients of plastic strain are predicted at the cavity wall.

5.2. Transformation hardening material (SIMT)

In Fig. 7 we show results for the variation of the ratios ρ/ρ_0 and σ_r/σ_Y with the normalized radial coordinate ξ. The dimensionless applied pressure considered is $P = 63$ (corresponding to $m = 0.28$). Theoretical predictions are compared with finite element results obtained for three different loading times (5 μs, 10 μs and 15 μs). As

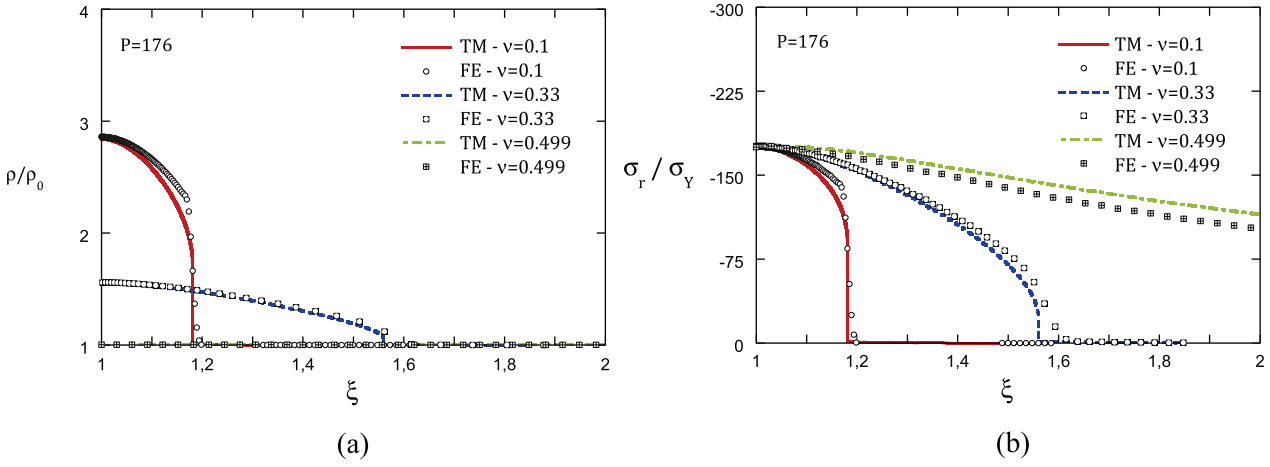

Fig. 10. Work hardening material (power law). Applied pressure $P = 176$. Variation along the normalized radial coordinate ξ of: (a) density ratio ρ/ρ_0 and (b) dimensionless radial stress σ_r/σ_Y. Comparison between theoretical model (TM) and finite element results (FE) for $\nu = 0.1$, $\nu = 0.33$ (reference material) and $\nu = 0.499$. Finite element results are shown for 3 μs.

for the work hardening material, agreement between the theoretical model and the finite element computations is observed and the difference between the finite element results for the different loading times, is hardly noticed. Implying that a self-similar field exists for a broader range of material response. The elastoplastic interface is located at $\xi_i \approx 3.30$ and the rigid/elastic front at $\xi_E \approx 4.43$ in agreement with predictions obtained from Eq. (13).

In Fig. 8 we examine results obtained for a higher level of the dimensionless cavitation pressure $P = 293.3$. This value of pressure leads to cavity expansion velocity $m = 0.66$ (see Fig. 3). This is above the upper limit in velocity ($m = 0.28$) for which the theoretical model can provide predictions. Hence, in Fig. 8 only the finite element results are presented for the variation of ρ/ρ_0 and σ_r/σ_Y along the normalized radial coordinate ξ. These are taken at three different loading times (2 μs, 3 μs and 4 μs) for which the cavitation velocity has already been reached. The results obtained for the three loading times lie within a single curve. We show that near the cavity $\rho/\rho_0 \approx 1.6$ and $\sigma_r/\sigma_Y = -293.3$. Moreover, the elastoplastic interface is located at $\xi_i \approx 1.6$. Close to that point we can see a steep slope in the curves $\rho/\rho_0 - \xi$ and $\sigma_r/\sigma_Y - \xi$ which characterizes the appearance of a plastic shock wave (at such a high cavitation ve-locities the plastic shock wave emerges close to the elastoplastic interface [11]). The rigid/elastic front is placed at $\xi_E \approx 1.84$ in agreement with predictions obtained from Eq. (13).

The next section of the analysis is devoted to explore the role played by different material aspects in the spherical cavity expansion.

6. Analysis and results: material aspects

6.1. The role played by the Poisson ratio

The effect of elastic compressibility in the dynamic cavitation process is investigated. Hence, in the present section results are presented for several values of the Poisson ratio with material hardening given in equation (4).

In Fig. 9 we show the relation between the dimensionless pressure P and the dimensionless cavity expansion velocity m.

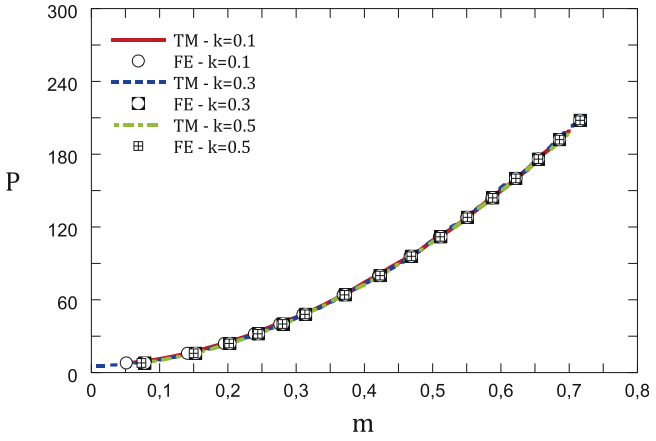

Fig. 12. Work hardening material (power law). Variation in dimensionless applied pressure P with dimensionless cavitation velocity m for $k = 0.1$, $k = 0.3$ and $k = 0.5$ (reference material). Comparison between theoretical model (TM) and finite element results (FE).

Results are presented for both theoretical and computational models considering $\nu = 0.1$, 0.33 and 0.499 within the range $0.05 \lesssim m \lesssim 0.75$. Agreement between predictions obtained from both methodologies is found. We show that the P–m curve is shifted upwards as ν increases. In other words, for a given value of applied pressure P the cavitation velocity m increases as ν decreases. This functional dependence of ν on the cavitation velocity is more noticeable as the cavitation pressure increases. The theoretical model predicts the first shock at $m = 0.39$ for $\nu = 0.1$ and at $m = 0.56$ for $\nu = 0.33$. It has to be noted that, approaching the incompressibility limit with $\nu = 0.499$, no plastic shock is detected within the range of cavitation velocities examined in this work. Moreover, the numerical computations show that the time to reach the steady field depends on the value of ν considered. This dependence is more noticeable as applied pressure increases. Thus for the highest applied pressure considered ($P = 208$) the time required to reach the steady field is ~0.3 μs for $\nu = 0.1$,

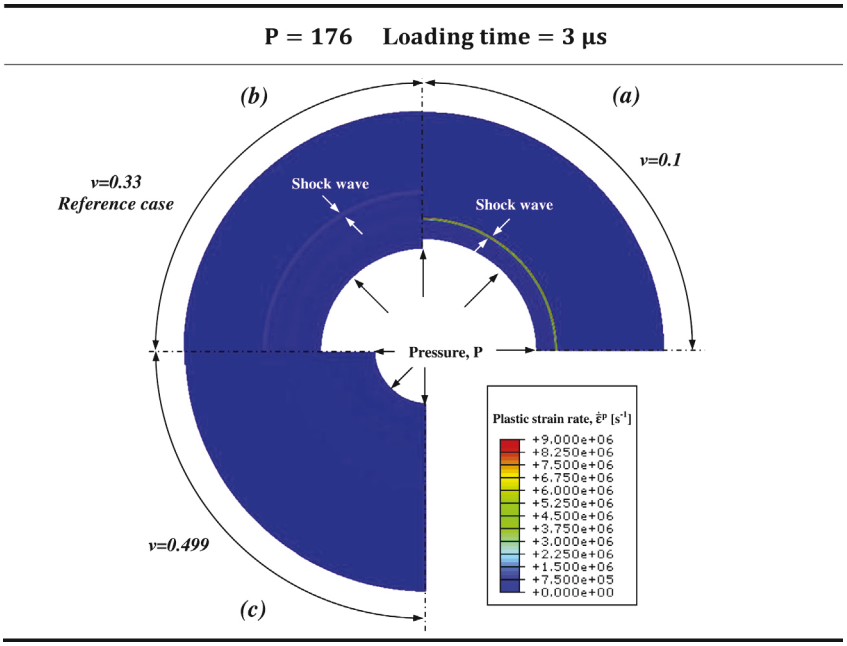

Fig. 11. Finite element results. Work hardening material (power law). Detail of the plastic strain rate contours in a zone surrounding the cavity. Cavitation fields for $P = 176$ and loading time 3 μs: (a) $\nu = 0.1$, (b) $\nu = 0.33$ (reference material) and (c) $\nu = 0.499$.

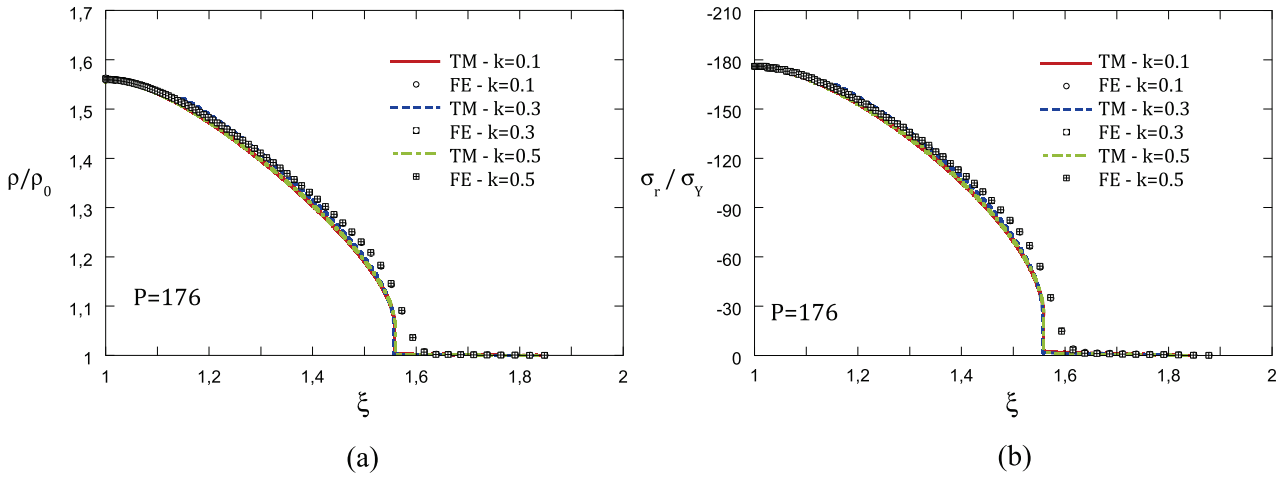

Fig. 13. Work hardening material (power law). Applied pressure $P = 176$. Variation along the normalized radial coordinate ξ of: (a) density ratio ρ/ρ_0 and (b) dimensionless radial stress σ_r/σ_Y. Comparison between theoretical (TM) model and finite element results (FE) for $k = 0.1$, $k = 0.3$ and $k = 0.5$ (reference material). Finite element results are shown for 3 μs.

~0.4 μs for $\nu = 0.33$ and ~1.0 μs for $\nu = 0.499$. The computational model therefore illustrates the key role played by elastic compressibility on the transient response that precedes the self-similar expansion.

Variation of the density ratio ρ/ρ_0 and the dimensionless radial stress σ_r/σ_Y along the normalized radial coordinate ξ is shown on Fig. 10 for $P = 176$ and the three values of the Poisson ratio considered in this section of the paper ($\nu = 0.1$, 0.33 and 0.499). We compare results obtained from the theoretical model and the finite element computations. The latter have been obtained at a loading time (3 μs) for which the steady state has already been reached. Therefore, we will not further elaborate on this issue in forthcoming analyses. Irrespective of the value of ν considered, there is a very close agreement between the analytical model and the numerical computations.

In Fig. 10(a) we see that near the cavity the density ratio is highly affected by the elastic compressibility: $\rho/\rho_0 \approx 2.9$ for $\nu = 0.1$, $\rho/\rho_0 \approx 1.6$ for $\nu = 0.33$ and $\rho/\rho_0 \approx 1.0$ (slightly above 1.0) for $\nu = 0.499$. Furthermore, the Poisson ratio has strong influence on the location of the elastoplastic interface. For $\nu = 0.1$ we observe at $\xi \approx 1.18$ a sudden drop in the ratio ρ/ρ_0 which represents the emergence of a plastic shock wave and for $\nu = 0.33$ the drop, located at $\xi \approx 1.6$, is more modest. For $\nu = 0.499$ the variation in density ratio is very small and no *sudden drop* is detected. The cavitation pressure is observed on Fig. 10(b) near the cavity wall where $P = -\sigma_r/\sigma_Y = 176$. The numerical simulations predict that the rigid/elastic front is placed at $\xi_E \approx 1.58$ for $\nu = 0.1$, at $\xi_E \approx 1.84$ for $\nu = 0.33$ and at $\xi_E \approx 25.25$ for $\nu = 0.499$. These values of ξ_E predicted by the numerical computations are in close agreement with the analytical predictions obtained from Eq. (13).

Fig. 11 presents detailed contours of plastic strain rate in the zone surrounding the cavity obtained via the finite element model for $P = 176$. We show results for $\nu = 0.1$, 0.33 and 0.499 taken at 3 μs. As expected, the radius of the cavity is greater as the value of ν decreases. Moreover, for $\nu = 0.1$ and 0.33 we observe a narrow band of high strain rates located at a certain distance from the cavity wall. This drastic increase in strain rate represents the plastic shock wave as discussed in Section 5. Within the band, higher strain rates are predicted in the case of $\nu = 0.1$ (9×10^6 s^{-1}) than in the case of $\nu = 0.33$ (9×10^5 s^{-1}). No shock wave is observed for $\nu = 0.499$ as expected when approaching the incompressibility limit.

6.2. The role played by strain hardening

In this section we examine specifically the role played by strain hardening on the dynamic cavitation fields. We consider separately each of the two hardening mechanisms described in Section 2.

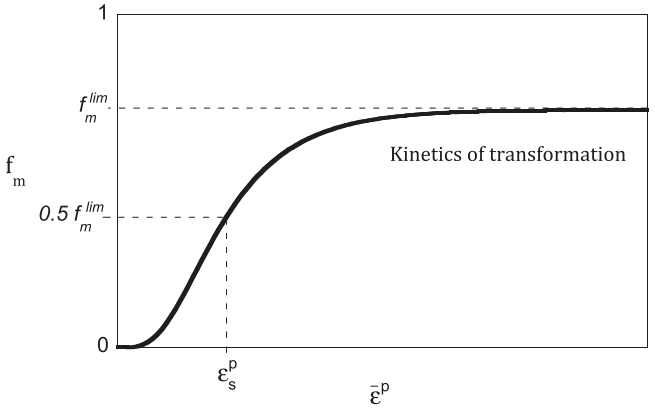

Fig. 14. Typical curve of the volume fraction of the martensite (f_m) as a function of the plastic strain ($\bar{\varepsilon}^p$) to show the role of the parameters $f_m^{\lim}$ and ε_s^p in the kinetics of martensitic transformation under isothermal conditions.

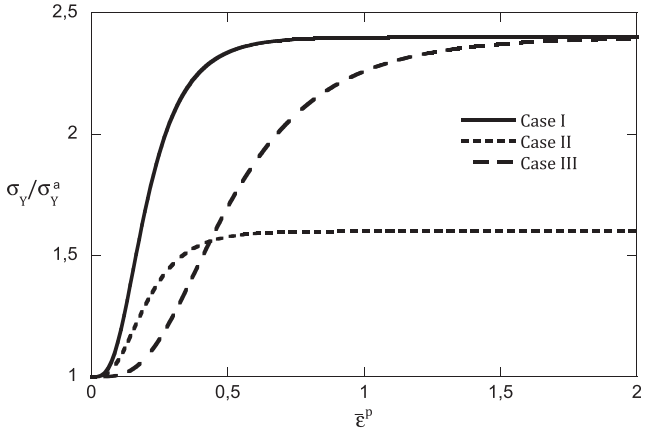

Fig. 15. Dimensionless flow stress (σ_Y/σ_Y^a) versus equivalent plastic strain ($\bar{\varepsilon}^p$) for case I ($\varepsilon_s^p = 0.2$, $f_m^{\lim} = 70\%$), case II ($\varepsilon_s^p = 0.2$, $f_m^{\lim} = 30\%$) and case III ($\varepsilon_s^p = 0.5$, $f_m^{\lim} = 70\%$).

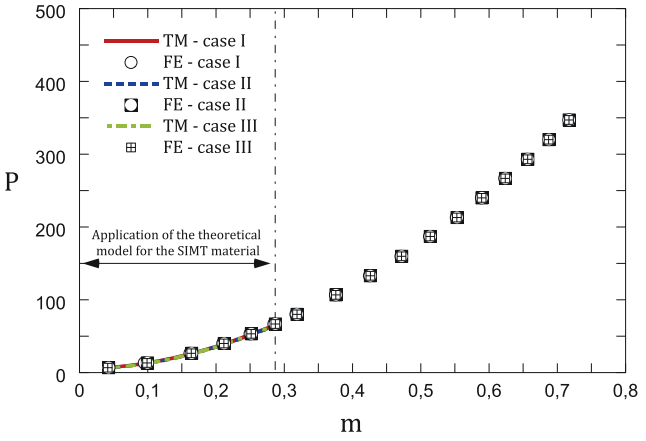

Fig. 16. Transformation hardening material (SIMT). Variation in dimensionless applied pressure P with dimensionless cavitation velocity m for case I (reference case), case II and case III. Comparison between theoretical model (TM) and finite element results (FE).

6.2.1. The work hardening effect

For the material hardening relation given in equation (4) we consider three values of the work hardening exponent $k = 0.1$, 0.3 and 0.5 with all other material parameters left with reference values (Table 2). The according dimensionless pressure P versus the dimensionless cavitation velocity m are shown on Fig. 12. Results from the theoretical model and the finite element simulations are presented within the range of cavity expansion velocities $0.05 \lesssim m \lesssim 0.75$ showing close agreement of theoretical results with the finite element simulation. As in Cohen et al. [11], we observe that the P–m curve hardly depends on the work hardening coefficient. Furthermore, irrespective of the considered value of k, the finite elements predict that the time required to reach the steady state is ~2.5 μs for the lowest cavitation pressure considered ($P = 8$) and ~0.4 μs for the highest ($P = 208$). According to those observations reported in Section 5, we emphasize here that the transient behavior which precedes the steady-state expansion seems to be hardly influenced by the inelastic behavior of the material (for the loading configuration and material behaviors selected in this paper).

In Fig. 13 we show the variation of density ratio ρ/ρ_0 and the dimensionless radial stress σ_r/σ_Y along the normalized radial coordinate ξ for $P = 176$. This value of applied pressure leads to cavitation velocity $m = 0.66$ (see Fig. 12). Theoretical and finite element results are compared for $k = 0.1$, $k = 0.3$ and $k = 0.5$. The computational results are taken at a loading time of 3 μs showing agreement between theory and finite element simulation. The work hardening coefficient hardly affects the curves $\rho/\rho_0 - \xi$ and $\sigma_r/\sigma_Y - \xi$. Irrespective of the value of k considered, the elasto-plastic interface is located at $\xi_i \approx 1.6$ and the rigid/elastic front is placed at $\xi_E \approx 1.86$. The work hardening exponent plays a minor role in the transient behavior as well as in the steady-state.

6.2.2. The transformation hardening effect

To investigate the constitutive sensitivity of the material with the hardening response described in equation (7), we consider two different sets of material parameters in addition to the reference values of α and β given in Table 3 (case I). First, it is instructive to illustrate the role of the parameters α and β in the material response. To that end we define the maximum fraction of transformed martensite – $f_m^{\lim}$ and the value of plastic deformation at half-transformation – ε_s^p, as illustrated on Fig. 14. While $f_m^{\lim}$ is solely determined by β, the value of ε_s^p is determined by both α and β. Whereas the parameter $f_m^{\lim}$ controls the value of the flow stress once the transformation is completed, the parameter ε_s^p controls the rate of transformation hardening. Next, we explore the role played by ε_s^p and $f_m^{\lim}$ on the process of dynamic cavitation, paying attention to three selected cases illustrated in Fig. 15. These are:

- Case I: $\varepsilon_s^p = 0.2$ and $f_m^{\lim} = 70\%$ ($\alpha = 7.943$, $\beta = 1.204$, values given in Table 3). This is considered as the reference case.
- Case II: $\varepsilon_s^p = 0.2$ and $f_m^{\lim} = 30\%$ ($\alpha = 9.154$, $\beta = 0.357$). In comparison with case I, now the fraction of martensite at saturation is decreased. This slows down the transformation hardening, and the saturation flow stress decreases.
- Case III: $\varepsilon_s^p = 0.5$ and $f_m^{\lim} = 70\%$ ($\alpha = 3.177$, $\beta = 1.204$). In comparison with case I, here the plastic strain at half-transformation increases. The plastic strain at which the transformation ends is delayed, decreasing the slope of the stress–strain curve. Notice that cases I and III have the same saturation flow stress.

In Fig. 16 we show the variation of P with m for cases I, II and III. Finite element computations are shown within the range $0.05 \lesssim m \lesssim 0.75$, whereas predictions of the theoretical model are limited to the range $0.05 \lesssim m \lesssim 0.28$. To be noted that $m \simeq 0.28$

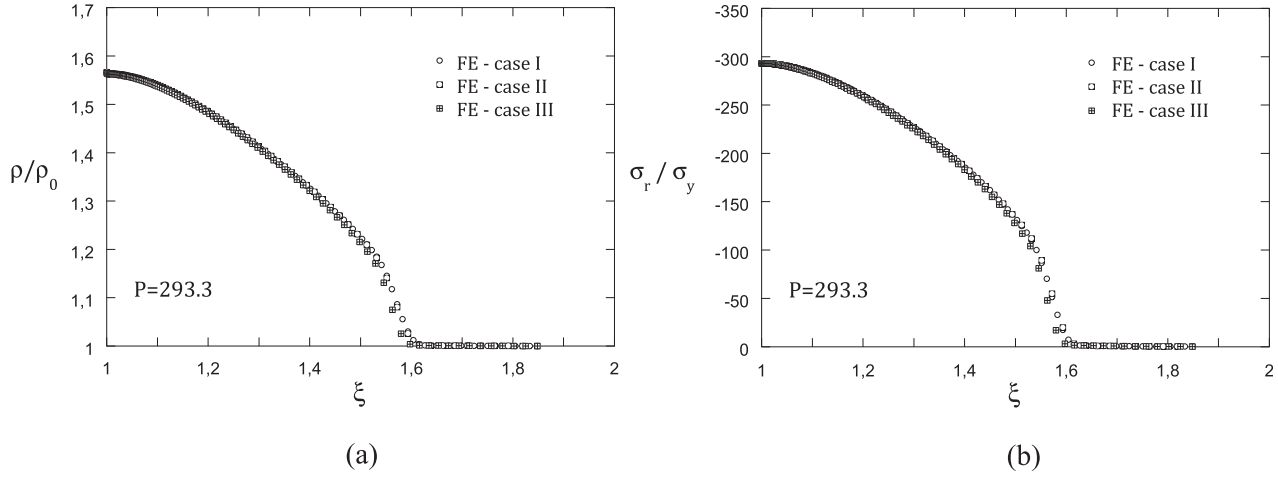

Fig. 17. Transformation hardening material (SIMT). Applied pressure $P = 293.3$. Variation along the normalized radial coordinate ξ of: (a) density ratio ρ/ρ_0 and (b) dimensionless radial stress σ_r/σ_Y. Finite element results (FE) for case I (reference case), case II and case III taken at 3 μs.

represents the cavitation velocity for which the theoretical model predicts the appearance of the first shock, imposing an upper limit to the predictions of the analytical model as discussed in Section 5. Within the range of cavitation velocities for which theoretical predictions are available, the agreement between the analytical model and numerical computations is observed. Moreover, it is shown that the transformation hardening barely affects the P–m relation. Furthermore, irrespective of the case considered the finite elements predict that the time required to reach the steady state is ~2.5 μs for the lowest cavitation pressure considered ($P = 13.3$) and ~0.4 μs for the highest ($P = 347$).

As opposed to the observations reported for different dynamic problems [20,19,27] in which the transformation hardening has large influence on the material response, we show here that strain induced martensitic transformation barely affects cavitation instability (at least for the loading configurations considered in this paper).

This behavior is further illustrated in Fig. 17 where we show the variation of the density ratio ρ/ρ_0 and the dimensionless radial stress σ_r/σ_Y along the normalized radial coordinate ξ for $P = 293.3$ (which corresponds to $m = 0.66$). Finite element results taken at a loading time of 3 μs are shown for cases I, II and III. Theoretical predictions are not shown because the cavitation velocity ($m = 0.66$) exceeds the upper limit for which the theoretical model admits solutions for this material behavior. Differences between the finite element curves $\rho/\rho_0 - \xi$ and $\sigma_r/\sigma_Y - \xi$ obtained for cases I, II and III are negligible. A plastic shock wave is observed near the elastoplastic interface $\xi \approx 1.6$. The rigid/elastic front is placed at $\xi_E \approx 1.84$ in agreement with results obtained from Eq. (13).

In Fig. 18 we present contours of volume fraction of martensite in the zone surrounding the cavity obtained via the finite element model for $P = 293.3$. Results are shown for cases I, II and III. Large values of strain are reached during the cavity expansion, favoring the martensitic transformation. Near the cavity we observe that the volume fraction of martensite is the maximum allowed $f_m^{\lim}$ for each case considered. However, we observe that large variations in the transformation hardening do not introduce substantial variations in the cavitation fields. Though several applications in which martensitic transformation enhances ductility and, in turn, enhances the energy absorption capabilities of the material under dynamic loading, the present analysis suggests that cavitation instabilities could not be impeded or controlled by *enhancing* the hardening response of the material. This result, together with the unrealistic stress levels observed in the steady cavitation state, suggest that incorporation of internal failure mechanisms, such as material porosity [12], pressure sensitivity [8] or a cut-off stress level, may be a key in design of materials with improved penetration resistance.

7. Concluding remarks

A numerical model to systematically evaluate the time dependent dynamic expansion of a spherical cavity, embedded in an unbounded medium and subjected to internal pressure is presented. Constitutive response is modeled by the standard principles of Huber–Mises plasticity, accounting for finite strains. Two distinct hardening mechanisms are considered; work hardening and strain induced martensitic transformation (SIMT). Despite the discretization, the numerical model is able to capture the propagation of spherical plastic shock waves, which were recently exposed in the theoretical study by Cohen et al. [11], and agrees with theoretical predictions at the steady-state limit. Though the theoretical analysis suggests that the appearance of a shock wave is involved with a finite jump in field variables, the inherent dampening of the numerical algorithm admits a smooth response with a thin band of steep gradients and increased strain rates at the shock. The thickness of the shock wave in the simulation is therefore controlled at a some extent by the numerical model. Nevertheless, other than the local discrepancies in the vicinity of the shock, agreement with the theoretical model is not compromised. Furthermore, it is conceivable that in real-life materials some strain rate effect necessarily exists implying that a jump in field variables is purely theoretical. Simulation results show that, for the material response considered and for instantaneous application of load,

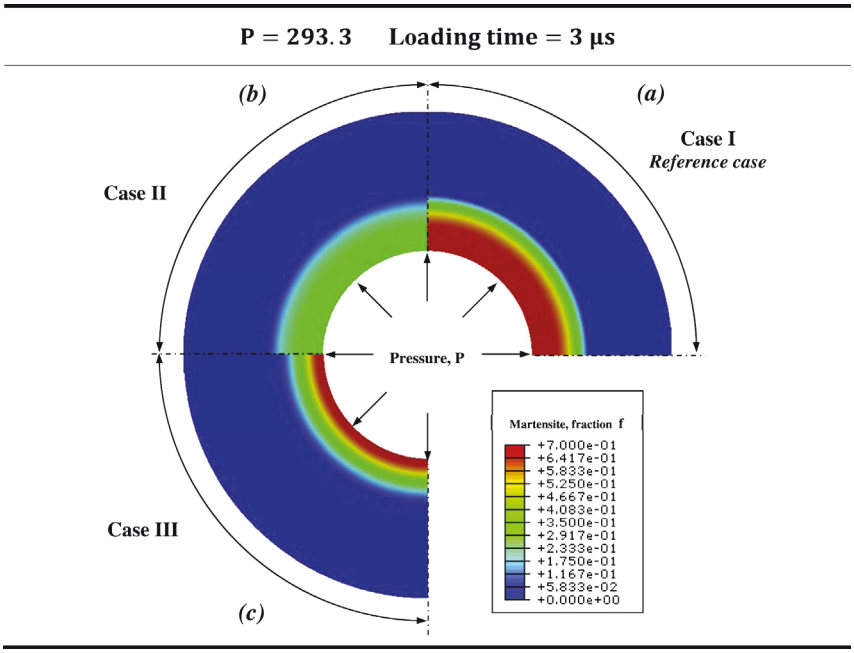

Fig. 18. Finite element results. Transformation hardening material (SIMT). Detail of the volume fraction of martensite in a zone surrounding the cavity. Cavitation fields for $P = 293.3$ and loading time 3 μs: (a) case I (reference case), (b) case II and (c) case III.

steady self-similar cavity expansion evolves at less than 3 μs, thus verifying the application of steady cavitation fields in prediction of hypervelocity penetration phenomena. It was also shown that the dynamic field is barely sensitive to the inelastic material response. That low sensitivity together with the unrealistically high levels of stress exhibited by the present model, implies that future design of structures with increased penetration resistance must account for more detailed material models. Namely, internal damage mechanisms such as material porosity or a cut-off hydrostatic stress level should be incorporated. While the theoretical model is limited to the steady-state response in absence of strain rate effects and thermo-mechanical coupling, the numerical model suggested here, and verified at the steady-state limit, facilitates future investigation of dynamic cavitation fields and shock wave propagation for more complicated material response.

Acknowledgments

The researchers of the University Carlos III of Madrid are indebted to the Ministerio de Ciencia e Innovación de España (Projects DPI/2011-24068 and DPI/2011-23191) for the financial support received which allowed conducting part of this work.

References

[1] Bishop R, Hill R, Mott N. The theory of indentation and hardness tests. Proc Phys Soc 1945;57:147–59.
[2] Ashby M, Blunt F, Bannister M. Flow characteristics of highly constrained metal wires. Acta Met 1989;37:1847–57.
[3] Zimberlin JA, Sanabria-DeLong N, Tew GN, Crosby AJ. Cavitation rheology for soft materials. Soft Matter 2007;3(6):763–7.
[4] Horgan C, Polignone D. Cavitation in nonlinearly elastic solids: a review. Appl Mech Rev 1995;48:471–85.
[5] Cohen T, Masri R, Durban D. Analysis of circular hole expansion with generalized yield criteria. Int J Solids Struct 2009;46:3643–50.
[6] Goodier J. On the mechanics of indentation and cratering in the solid targets of strain hardening metal by impact of hard and soft spheres. In: Proceedings of the 7th symposium on hypervelocity impact, vol. III; 1965. pp. 215–59.
[7] Hunter SC, Crozier RJM. Similarity solution for the rapid uniform expansion of a spherical cavity in a compressible elastic-plastic solid. Q J Mech Appl Math 1968;21:467–86.
[8] Durban D, Fleck NA. Spherical cavity expansion in a Drucker-Prager solid. J Appl Mech 1997;64:743–50.
[9] Durban D, Masri R. Dynamic spherical cavity expansion in a pressure sensitive elastoplastic medium. Int J Solids Struct 2004;41:5697–716.
[10] Masri R, Durban D. Dynamic spherical cavity expansion in an elastoplastic compressible mises solid. J Appl Mech 2004;72:887–98.
[11] Cohen T, Masri R, Durban D. Shock waves in dynamic cavity expansion. J Appl Mech 2010;77:041009.
[12] Cohen T, Durban D. Hypervelocity cavity expansion in porous elastoplastic solids. J Appl Mech 2013;80:011017.
[13] Ortiz M, Molinari A. Effect of strain hardening and rate sensitivity on the dynamic growth of a void in a plastic material. J Appl Mech 1992;59(1): 48–53.
[14] Andersson R. Deformation characteristics of stainless steels [Ph.D. thesis]. Sweden: Lulea University of Technology; 2005.
[15] Langdon GS, Schleyer GK. Inelastic deformation and failure of profiled stainless steel blast wall panels. Part I: experimental investigations. Int J Impact Eng 2005;31:341–69.
[16] Langdon GS, Schleyer GK. Inelastic deformation and failure of profiled stainless steel blast wall panels. Part II: analytical modelling considerations. Int J Impact Eng 2005;31:371–99.
[17] Bleck W, Larour P, B¨aumer A. High strain rate tensile testing of modern car body steels. Mater Forum 2005;29:21–8.
[18] Sato K, Inazumi T, Yoshitake A, Liu S. Effect of material properties of advanced high strength steels on bending crash performance of hat-shaped structure. Int J Impact Eng 2013;54:1–10.
[19] Rodríguez-Martínez JA, Rusinek A, Pesci R, Zaera R. Experimental and numerical analysis of the martensitic transformation in AISI 304 steel sheets subjected to perforation by conical and hemispherical projectiles. Int J Solids Struct 2013;50:339–51.
[20] Rodríguez-Martínez JA, Rittel D, Zaera R, Osovski S. Finite element analysis of AISI 304 steel sheets subjected to dynamic tension: the effects of martensitic transformation and plastic strain development on flow localization. Int J Impact Eng 2013;53:206–16.
[21] Zaera R, Rodríguez-Martínez JA, Vadillo G, Fern´andez-S´aez J. Dynamic necking in materials with strain induced martensitic transformation. J Mech Phys Solids 2014;64:316–37.
[22] Courant R, Friedrichs KO. Supersonic flow and shock waves, vol. 21. Springer; 1976.
[23] Cohen T, Durban D. Longitudinal shock waves in solids: the piston shock analogue. Proc Royal Soc A – Math, Phys Eng Sci 2014;470(2164):20130061.
[24] Rosenberg Z, Dekel E. A numerical study of the cavity expansion process and its application to long-rod penetration mechanics. Int J Impact Eng 2008;35: 147–54.
[25] Masri R, Durban D. Deep penetration analysis with dynamic cylindrical cavitation fields. Int J Impact Eng 2009;36(6):830–41.
[26] Olson GB, Cohen M. Kinetics of strain-induced martensitic nucleation. Metall Trans A 1975;6A:791–5.
[27] Zaera R, Rodríguez-Martínez JA, Casado A, Fern´andez-S´aez J, Rusinek A, Pesci R. A constitutive model for analyzing martensite formation in austenitic steels deforming at high strain rates. Int J Plast 2012;29:77–101.
[28] Simulia. ABAQUS/Explicit user's manual. Providence, USA: Dassault Syst`emes; 2010. version 6.10.
[29] Simo´ JC, Hughes TJR. Computational inelasticity. New York: Springer; 1998.
[30] Doghri I. Mechanics of deformable solids: linear and nonlinear, analytical and computational aspects. Berlin: Springer; 2000.
[31] Zukas JA, Scheffer DR. Practical aspects of numerical simulations of dynamic events: effects of meshing. Int J Impact Eng 2000;24:925–45.